

Perfect Andreev reflection due to the Klein paradox in a topological superconducting state

Seunghun Lee^{1,2}, Valentin Stanev^{1,2,3}, Xiaohang Zhang^{1,2}, Drew Stasak¹, Jack Flowers¹, Joshua S. Higgins^{2,4}, Sheng Dai⁵, Thomas Blum⁶, Xiaoqing Pan^{5,6,7}, Victor M. Yakovenko^{3,4,8}, Johnpierre Paglione^{2,4}, Richard L. Greene^{2,4}, Victor Galitski^{3,4,8} & Ichiro Takeuchi^{1,2,4*}

In 1928, Dirac proposed a wave equation to describe relativistic electrons¹. Shortly afterwards, Klein solved a simple potential step problem for the Dirac equation and encountered an apparent paradox: the potential barrier becomes transparent when its height is larger than the electron energy. For massless particles, backscattering is completely forbidden in Klein tunnelling, leading to perfect transmission through any potential barrier^{2,3}. The recent advent of condensed-matter systems with Dirac-like excitations, such as graphene and topological insulators, has opened up the possibility of observing Klein tunnelling experimentally^{4–6}. In the surface states of topological insulators, fermions are bound by spin–momentum locking and are thus immune from backscattering, which is prohibited by time-reversal symmetry. Here we report the observation of perfect Andreev reflection in point-contact spectroscopy—a clear signature of Klein tunnelling and a manifestation of the underlying ‘relativistic’ physics of a proximity-induced superconducting state in a topological Kondo insulator. Our findings shed light on a previously overlooked aspect of topological superconductivity and can serve as the basis for a unique family of spintronic and superconducting devices, the interface transport phenomena of which are completely governed by their helical topological states.

Klein’s gedanken experiment illustrates the intrinsic connection between particles and antiparticles in relativistic quantum mechanics, and observing this connection ostensibly requires velocities close to the speed of light². However, several condensed-matter systems have recently emerged as unexpected platforms for the study of relativistic effects. In materials such as graphene and topological insulators, the Dirac equation provides an effective low-energy description of band electrons^{4,5}. In graphene heterostructures, the modulation of conductance as functions of electron trajectory and electrostatic potential profile has previously been used as a vehicle for the investigation of Klein tunnelling^{5,7,8}. Here we demonstrate an alternative way in which to directly observe Klein tunnelling using a topological insulator. We use point-contact Andreev reflection (PCAR) measurements at the interface between a normal metal and a topological superconducting state (that is, the superconducting surface states of a topological insulator). The perfect transmission of electrons through a finite barrier manifests as an observed doubling of the conductance within the superconducting gap (Δ). This doubling of the conductance is due to the conservation of charge, spin and momentum in the Andreev reflection process, which requires that a positively charged hole with opposite spin and momentum to that of the electron is left behind^{9–11}. In real experiments, however, enhancement of the conductance is easily suppressed by various inevitable scattering mechanisms that arise from non-ideal interface conditions, and complete doubling of the conductance is very rarely observed. The extreme sensitivity to scattering makes Andreev reflection a unique tool for the detection of Klein tunnelling.

Spin–momentum locking of the Dirac states prohibits the reflection of an incident electron normal to the interface, irrespective of the microscopic details of the interface¹². It results in the complete absence of backscattering, and thus gives rise to topologically protected perfect Andreev reflection that manifests as an exact doubling of the conductance. Such a direct probe for the observation of Dirac particles could lead to a better understanding of their condensed matter implementations, and greater use of their properties in quantum transport devices.

To investigate how the presence of Dirac states at the surface of a topological insulator affects the processes of particle transport governed by Andreev reflection, we used a tip made of a platinum-iridium alloy (PtIr) to form a point-contact interface with a topological-insulator film in which superconductivity is induced through the proximity effect (Fig. 1a). We used heterostructures consisting of samarium hexaboride (SmB_6) and yttrium hexaboride (YB_6) to induce superconductivity in the Dirac surface states of SmB_6 . SmB_6 is a topological Kondo insulator, in which the bulk gap at low temperatures ensures the existence of an insulating bulk sandwiched by topologically protected conducting surface layers^{13–18}. This is a critical prerequisite for the observation of effects that originate solely from the topologically protected states^{19,20}. The use of the isostructural rare-earth-hexaboride superconductor YB_6 (with a critical temperature, T_c , of around 6.3 K) as the layer underneath SmB_6 enables the fabrication, by sequential high-temperature growth, of a pristine SmB_6/YB_6 interface, which is necessary for achieving a robust proximity effect²¹ (see Methods and Extended Data Figs. 1, 2 for details).

As theoretically predicted⁶ and experimentally confirmed²⁰, the superconducting proximity effect that occurs in such topological insulator/superconductor heterostructures creates helical Cooper pairing on the surface of a topological insulator. Owing to the constraints imposed by the two-dimensional surface states and the insulating bulk, incoming electrons with finite momenta perpendicular to the surface (p_z) do not participate in the transport at the interface between a normal metal and topological insulator/superconductor heterostructure²². Thus, the PtIr- SmB_6/YB_6 contact creates an interface at which only in-plane transport (that is, momentum parallel to the plane of the surface states, so $p_z = 0$) is allowed (Fig. 1a). In addition, induced spin–momentum locking in a normal metal in contact with a topological insulator has previously been observed as a result of the topological proximity effect^{23,24}. Owing to the spin–momentum locking on both sides, incident electrons are forbidden from reflecting back (Fig. 1b). The perfect electron transmission to superconducting SmB_6 and the concomitant hole generation result in the observed doubling of conductance for energies within the proximity-induced Δ .

SmB_6/YB_6 heterostructures were analysed by point-contact spectroscopy at 2 K. For SmB_6 layers with thicknesses in the range of 20 to 30 nm, normalized differential-conductance (dI/dV) curves showed doubling of the conductance within the bias voltage corresponding

¹Department of Materials Science and Engineering, University of Maryland, College Park, MD, USA. ²Center for Nanophysics and Advanced Materials, University of Maryland, College Park, MD, USA. ³Joint Quantum Institute, University of Maryland, College Park, MD, USA. ⁴Department of Physics, University of Maryland, College Park, MD, USA. ⁵Department of Materials Science and Engineering, University of California, Irvine, CA, USA. ⁶Department of Physics and Astronomy, University of California, Irvine, CA, USA. ⁷Irvine Materials Research Institute, University of California, Irvine, CA, USA. ⁸Condensed Matter Theory Center, University of Maryland, College Park, MD, USA. *e-mail: takeuchi@umd.edu

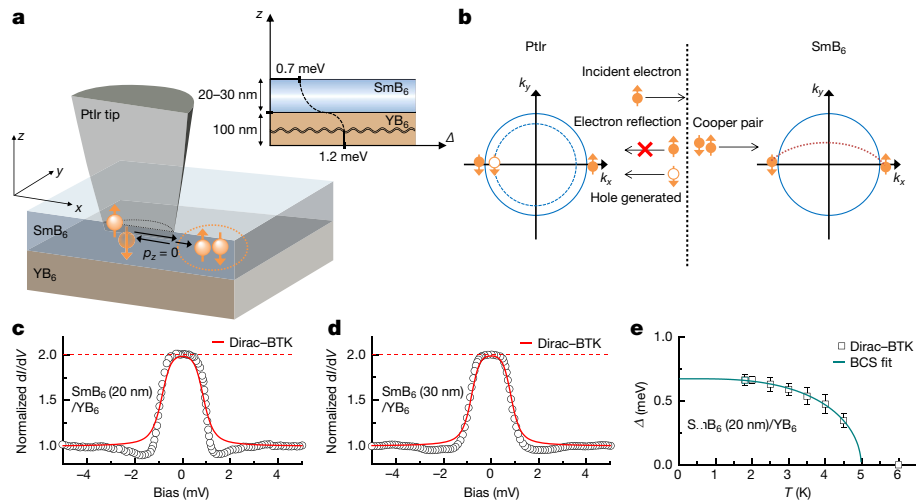


Fig. 1 | Perfect Andreev reflection due to the Klein paradox.

a, Schematic of PCAR measurement on SmB_6/YB_6 heterostructures. Owing to the lack of bulk states in SmB_6 , only electrons with momentum parallel to the plane of the surface states of SmB_6 (that is, $p_z = 0$) contribute to transport. The inset shows variation of Δ in a SmB_6 (20–30 nm)/ YB_6 heterostructure. There is a finite Δ in the top conducting surface of SmB_6 . **b**, Andreev reflection process at the interface between PtIr and superconducting SmB_6 . The surface of SmB_6 has topologically protected helical states exhibiting spin–momentum locking. Irrespective of barrier height, normal electron reflection is not allowed because it requires a spin flip. **c, d**, Perfect Andreev reflection due to Klein tunnelling, indicated

to the induced Δ . As seen in Figs. 1c, 1d, the observed doubling of the conductance is exact within the uncertainty due to the fitting procedure (see Methods and Extended Data Fig. 5). In this regime, the SmB_6 layer is sufficiently thick to have fully developed topologically protected surface states, while the superconducting proximity effect from the YB_6 can still be observed at the top surface (as depicted in the inset of Fig. 1a).

The best theoretical fit to the data is based on the Blonder, Tinkham and Klapwijk (BTK) theory⁹ (see below) and results in a proximity-induced Δ of around 0.7 meV; as expected, this is smaller than the bulk Δ of YB_6 (≈ 1.3 meV)²⁵. The temperature dependence and magnetic-field dependence of a dI/dV spectrum were measured on a separately fabricated Au- SmB_6/YB_6 structure (see Methods and Extended Data Figs. 3, 7), in which the junction comprises a thin film of gold. The obtained temperature dependence of Δ shows the Bardeen–Cooper–Schrieffer behaviour, as expected (Fig. 1e); this confirms that the enhancement of conductance seen in the dI/dV spectrum is due to the proximity-induced superconductivity on the topologically protected top surface of SmB_6 .

The transmission and reflection of particles through an interface between a normal metal and a superconductor is described by the BTK theory⁹. A dimensionless parameter Z represents the interfacial barrier strength, which reduces the transparency of the interface: perfect conductance doubling within Δ thus requires $Z \approx 0$ in the standard BTK theory. However, we show below that the superconductivity induced in the topologically protected surface states of SmB_6 inhibits electron reflection and cancels the effect of the barrier strength. Thus, even for a finite Z in PtIr- SmB_6/YB_6 point contact there can be perfect electron transmission, which is directly discernible by the conductance doubling. Describing this phenomenon requires modification of the BTK theory to account for the role of the Dirac surface states of SmB_6 in the dI/dV spectrum, which is henceforth referred to as the Dirac–BTK theory.

The perfect Andreev reflection is a direct consequence of the presence of topologically protected surface states as well as the absence of a bulk conduction channel. On the basis of our systematic study, when the thickness of the SmB_6 film is less than about 20 nm^{21,26} the

by exact doubling of the normalized differential conductance (dI/dV), is observed in the point-contact spectroscopy of PtIr- SmB_6 (20 nm)/ YB_6 (100 nm) (**c**) and PtIr- SmB_6 (30 nm)/ YB_6 (100 nm) (**d**) heterostructures measured at 2 K. The red lines are fits to the experimental data using a BTK model modified with a Dirac Hamiltonian (Dirac–BTK) with $\Delta = 0.75 \pm 0.06$ meV (**c**) and $\Delta = 0.73 \pm 0.05$ meV (**d**). **e**, The temperature-dependent Δ (extracted using the Dirac–BTK model) from a Au- SmB_6 (20 nm)/ YB_6 structure in which a gold thin film was used to form the junction (see Methods, Extended Data Fig. 3), displaying Bardeen–Cooper–Schrieffer behaviour (cyan line).

effect of hybridization of the top and bottom surface states becomes pronounced, which opens a gap in the dispersion of the surface states and weakens the topological protection^{20,27} (Fig. 2a). This accounts for the reduced conductance enhancement that is observed upon contact with the SmB_6 (10 nm)/ YB_6 heterostructure at 2 K (Fig. 2b). To confirm the role of the robust bulk gap of SmB_6 in our observation, we also performed PCAR measurements on $\text{Sm}_{1-x}\text{Y}_x\text{B}_6$ (20 nm)/ YB_6 heterostructures, in which samarium is partially substituted by yttrium in the top layer to modify its electronic structure. Yttrium ions are expected to generate conducting bulk states, which in turn give rise to transport channels that are not subjected to spin–momentum locking (see Methods and Extended Data Fig. 4). As expected, point-contact spectra of $\text{Sm}_{0.8}\text{Y}_{0.2}\text{B}_6/\text{YB}_6$ and $\text{Sm}_{0.5}\text{Y}_{0.5}\text{B}_6/\text{YB}_6$ heterostructures at 2 K show a conductance enhancement at zero bias of around 1.5, which is substantially lower than an exact doubling (Fig. 2c, d).

When the surface of a YB_6 film is probed directly—that is, with no SmB_6 layer on top—the point-contact spectrum at 2 K displays an entirely different characteristic: the junction is now in the regime in which tunnelling has a substantial contribution, resulting in reduced conductance in the gap region of YB_6 with a substantial barrier strength at the interface ($Z \approx 1$, extracted using the standard BTK model) (Fig. 2e). The gap value ($\Delta \approx 1.3$ meV) determined from the fit is consistent with the full superconducting gap of YB_6 ²⁵. At the other limit, when the thickness of SmB_6 is greater than 40 nm, the dI/dV spectrum at 2 K (Fig. 2f) does not show any features corresponding to proximity-induced superconductivity. Instead, the entire dI/dV spectrum shows Fano resonance—a familiar signature of the Kondo lattice physics of bulk SmB_6 ¹⁶.

To illustrate the uniqueness of the perfect Andreev reflection observed here, we surveyed the open literature on PCAR measurements performed on various superconductors. Figure 3 shows plots of normalized dI/dV at zero bias (that is, conductance enhancement) against Z (obtained from the BTK fit) from 44 reports selected from 250 publications on PCAR measurements (see Methods; the list of publications and other details are provided in Supplementary Table). The general trend is well captured by the standard BTK model (cyan line). To the best of our knowledge there are only two studies in the literature,

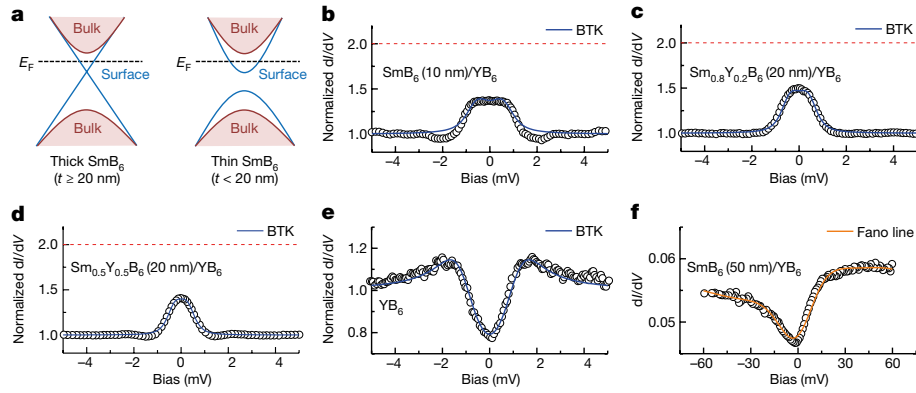


Fig. 2 | Sensitivity of perfect Andreev reflection to compromised topological superconductivity. When superconductivity in the surface states of SmB_6/YB_6 is modified by changing the thickness or the composition of the SmB_6 layer, the conductance doubling is suppressed. **a**, Band structures of different thicknesses of SmB_6 . **b**, Point-contact spectrum of a SmB_6 (10 nm)/ YB_6 heterostructure. Reduced conductance at zero bias (normalized $dI/dV \approx 1.4$) is observed. **c–e**, Point-contact spectra of yttrium-substituted SmB_6 ($\text{Sm}_{1-x}\text{Y}_x\text{B}_6$ (20 nm))/ YB_6 heterostructures with $x = 0.2$ (**c**) and $x = 0.5$ (**d**) and of the YB_6 layer only (**e**). The blue lines are best fits to the standard BTK theory: for **b**, $Z = 0.42 \pm 0.10$,

$\Delta = 0.59 \pm 0.10$ meV and $\Gamma \leq 0.16$ meV; for **c**, $Z = 0.35 \pm 0.09$, $\Delta = 0.49 \pm 0.05$ meV and $\Gamma \leq 0.08$ meV; for **d**, $Z = 0.42 \pm 0.06$, $\Delta = 0.30 \pm 0.04$ meV and $\Gamma \leq 0.04$ meV; for **e**, $Z = 1.04 \pm 0.06$, $\Delta = 1.24 \pm 0.08$ meV and $\Gamma = 0.60 \pm 0.04$ meV. Z and Γ are the interface barrier strength and the broadening parameter, respectively. **f**, The point-contact spectrum of a SmB_6 (50 nm)/ YB_6 exhibits an asymmetric Fano-like spectrum due to the inherent Kondo-lattice electronic structure of SmB_6 . The orange line is the best fit to the Fano-line shape¹⁶. All point-contact spectra were obtained at 2 K.

both on Nb-Cu junctions^{28,29}, that report an observed normalized dI/dV at zero bias of greater than 1.9. A detailed explanation and comparison between our PtIr- SmB_6 (20–30 nm)/ YB_6 point-contact spectra and the reported Nb-Cu point-contact spectra (Extended Data Fig. 8) are provided in Methods.

According to the standard BTK theory, the observed perfect conductance doubling implies that, when the thicknesses of the SmB_6 layer are in the range of 20 to 30 nm, $Z \approx 0$ for contacts to the SmB_6/YB_6 heterostructures. However, we think that the factors dictated by the materials are similar or identical for all heterostructures studied here, including the 10-nm-thick SmB_6 and the yttrium-substituted SmB_6 heterostructures. Thus, we expect materials-dictated Z for junctions that exhibit perfect Andreev reflection to be approximately 0.4—an average of the extracted Z values for the contacts with heterostructures that do not have complete topological protection (navy pentagon in Fig. 3).

Now we consider the mechanism of the perfect Andreev reflection for finite Z . To describe the transmission and the reflection processes at an interface between a normal metal and a superconducting topological insulator (which in our case is a topological insulator with proximity-induced superconductivity in the surface states), we modify the standard BTK theory⁹—which describes the transport at a normal metal/conventional superconductor interface—by considering the unique properties of a superconducting topological insulator. The key factor in the modification is the interplay of the spin and the momentum of the electrons in the surface states of SmB_6 —a consequence of the non-trivial topology of the bulk band structure. These states are described by the Dirac Hamiltonian that displays spin-momentum locking, as manifested in helicity. As first shown by Klein, this can lead to perfect transmission through an arbitrarily large potential barrier: normal reflection of a Dirac particle requires a complete spin flip and thus is forbidden. The presence of such perfectly transmitting channels at the boundary between a topological material and a topological superconductor nullifies the effects of the boundary barrier, including the Fermi velocity mismatch, thus leading to perfect Andreev reflection—that is, the doubling of the conductance within Δ in a dI/dV spectrum¹². Bulk PtIr is a normal metal. However, the topological proximity effect can render PtIr topologically nontrivial when in contact with SmB_6 , thereby satisfying the necessary condition for the perfect Andreev reflection^{23,24}: the contact with the SmB_6 surface breaks the degeneracy of the two helicities in the PtIr tip, and in the region adjacent to the interface only the states matching the helicity on the SmB_6 side are allowed. The strong spin-orbit coupling

of PtIr itself can also play a part in this process (see Supplementary Discussion for details).

We thus model the PtIr- SmB_6 boundary as a line dividing the normal and the superconducting regions in the plane of the SmB_6 surface states. At the boundary, we add a delta-function potential term $U(x) = U_0\delta(x)$ modelling the barrier at the interface, typically represented by the dimensionless barrier-strength parameter Z ($Z \equiv U_0/\hbar v_F^S$), where \hbar is the reduced Planck's constant and v_F^S is the Fermi velocity on the SmB_6 side. The Dirac Hamiltonian on the superconducting topological-insulator side can be written (in $\Psi = [\psi_{\uparrow, \varepsilon, p}, \psi_{\downarrow, \varepsilon, p}, \psi_{\uparrow, -\varepsilon, -p}^*, \psi_{\downarrow, -\varepsilon, -p}^*]$ basis) as³⁰

$$H_{\text{hetero}} = \begin{pmatrix} v_F \mathbf{p} \cdot \boldsymbol{\sigma} - \sigma_0 \mu + \sigma_0 U(x) & i\sigma_y \Delta \\ -i\sigma_y \Delta & v_F \mathbf{p} \cdot \boldsymbol{\sigma}^* + \sigma_0 \mu - \sigma_0 U(x) \end{pmatrix}$$

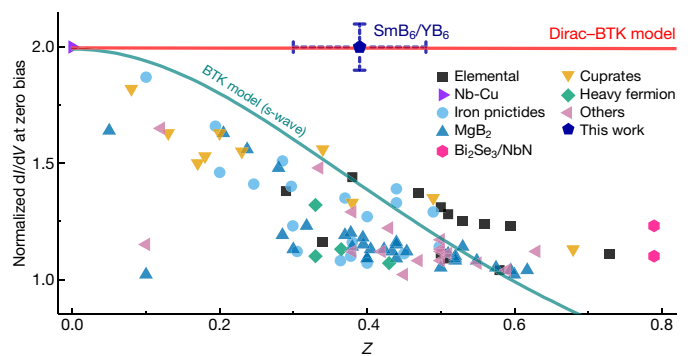


Fig. 3 | Andreev reflection process under the Dirac Hamiltonian. A survey of reported normalized dI/dV at zero bias (that is, conductance enhancement) plotted against Z (that is, the dimensionless barrier strength parameter) for PCAR measurements on various superconductors (see Supplementary Table for references and plotted values). The theoretical Z -dependent normalized dI/dV at zero bias, calculated by the standard BTK (cyan) and the Dirac-BTK models (red) are shown (see Methods and Extended Data Fig. 6 for details). Simulation parameters: $T = 2$ K; $\Delta = 1$ meV. For PtIr- SmB_6 (20–30 nm)/ YB_6 junctions that display perfect Andreev reflection (normalized $dI/dV = 2$), we assume that the Z value is similar to that of junctions with other heterostructures in this study that do not have perfect Andreev reflection (thin SmB_6 (10 nm) and Y-substituted SmB_6); that is, $Z = 0.39 \pm 0.09$, with error bars reflecting the fitting procedure (navy pentagon, this work).

where \mathbf{p} is momentum in the x - y plane, μ is the chemical potential and $\sigma \equiv [\sigma_x, \sigma_y]$ ($\{\sigma_0, \sigma_x, \sigma_y, \sigma_z\}$ is the set of the identity and the Pauli matrices in the spin space). Δ is the proximity-induced superconducting gap in the top surface of the SmB_6 layer.

Using the appropriate boundary condition for a metal with single helicity (see Supplementary Discussion for details) and for energies close to the Fermi level, we can derive analytically the coefficients for each allowed process: r_e , reflection as an electron; r_h , Andreev reflection; t_e , transmission as an electron-like particle; t_h , transmission as a hole-like particle. These coefficients depend on the following: the energy (or bias voltage V); θ_k , the angle of incidence measured from the normal to the boundary; Z , which encodes the effects of the boundary barrier; and v_F^S/v_F^N , the Fermi velocity mismatch, where v_F^N is the Fermi velocity on the normal metal (PtIr) side.

The conductance ($G = dI/dV$) through the interface is then given (at zero temperature) by:

$$G = \frac{dI}{dV} = G_0 \int_{-\chi}^{\chi} (1 - |r_e(\theta_k)|^2 + |r_h(\theta_k)|^2) f_{\theta_k} \cos\theta_k d\theta_k \quad (1)$$

where f_{θ_k} models the angular distribution of the incoming electrons, $\chi \equiv \arcsin(v_F^N/v_F^S)$, and G_0 is a constant. The angular dependence of r_e goes as $r_e(\theta_k) \approx \sin\theta_k$; reflection as an electron at $\theta_k = 0$ requires a spin flip, which is forbidden by time-reversal symmetry, and thus $r_e(\theta_k = 0) = 0$. Reproducing the observed perfect conductance doubling requires a rather narrow f_{θ_k} centred around $\theta_k = 0$ (see Supplementary Discussion for details). In this quasi-one-dimensional case, there is perfect transmission irrespective of the barrier height and Fermi velocity mismatch—the essence of Klein tunnelling (red line in Fig. 3). For $|eV| < \Delta$ (that is, energies below the superconducting gap) this leads to $r_h(\theta_k \approx 0) = 1$, whereas for $|eV| \gg \Delta$ we have $r_h = 0$; combining these two results with equation (1) immediately leads to conductance doubling: $G(|eV| < \Delta)/G(|eV| \gg \Delta) = 2$.

In summary, we have observed perfect Andreev reflection—a manifestation of Klein tunnelling—using proximity-induced superconductivity in a three-dimensional topological insulator. Despite the formal similarity between Dirac excitations in graphene and in topological insulators, there are important differences between the two with respect to Klein tunnelling. In graphene, the degeneracy between sublattices of the honeycomb structure is crucial, whereas in topological insulators it is the time-reversal symmetry that directly prohibits backscattering. The unusual combination of the topologically protected surface states and the lack of bulk states in thin layers of SmB_6 films has facilitated the observation of perfect Andreev reflection due to Klein tunnelling. Perfect transmission renders transport of individual electrons across an interface dissipation-less, regardless of the origins of the potential barrier and its variation—an attractive attribute for many device applications including quantum information processing³¹ and high-sensitivity detectors³². We foresee Klein tunnelling in topological insulators to be a platform for the exploration of various interface transport phenomena, including perfect spin-filters as governed by unadulterated spin–momentum locking³³.

Online content

Any methods, additional references, Nature Research reporting summaries, source data, statements of data availability and associated accession codes are available at <https://doi.org/10.1038/s41586-019-1305-1>.

Received: 25 June 2018; Accepted: 16 April 2019;
Published online 19 June 2019.

- Dirac, P. A. M. The quantum theory of the electron. *Proc. R. Soc. Lond. A* **117**, 610–624 (1928).
- Klein, O. Die reflexion von Elektronen an einem Potentialsprung nach der relativistischen Dynamik von Dirac. *Z. Phys.* **53**, 157–165 (1929).
- Calogeracos, A. & Dombey, N. History and physics of the Klein paradox. *Contemp. Phys.* **40**, 313–321 (1999).
- Hasan, M. Z. & Kane, C. L. Colloquium: topological insulators. *Rev. Mod. Phys.* **82**, 3045–3067 (2010).

- Beenakker, C. W. J. Colloquium: Andreev reflection and Klein tunneling in graphene. *Rev. Mod. Phys.* **80**, 1337–1354 (2008).
- Fu, L. & Kane, C. L. Superconducting proximity effect and Majorana fermions at the surface of a topological insulator. *Phys. Rev. Lett.* **100**, 096407 (2008).
- Stander, N., Huard, B. & Goldhaber-Gordon, D. Evidence for Klein tunneling in graphene p–n junctions. *Phys. Rev. Lett.* **102**, 026807 (2009).
- Young, A. F. & Kim, P. Quantum interference and Klein tunneling in graphene heterojunctions. *Nat. Phys.* **5**, 222–226 (2009).
- Blonder, G. E., Tinkham, M. & Klapwijk, T. M. Transition from metallic to tunneling regimes in superconducting microconstrictions: Excess current, charge imbalance, and supercurrent conversion. *Phys. Rev. B* **25**, 4515–4532 (1982).
- Daghero, D. & Gonnelli, R. S. Probing multiband superconductivity by point-contact spectroscopy. *Supercond. Sci. Technol.* **23**, 043001 (2010).
- Lee, W.-C. & Greene, L. H. Recent progress of probing correlated electron states by point contact spectroscopy. *Rep. Prog. Phys.* **79**, 094502 (2016).
- Adroguer, P. et al. Probing the helical edge states of a topological insulator by Cooper-pair injection. *Phys. Rev. B* **82**, 081303 (2010).
- Dzero, M., Sun, K., Coleman, P. & Galitski, V. Theory of topological Kondo insulators. *Phys. Rev. B* **85**, 045130 (2012).
- Syers, P., Kim, D., Fuhrer, M. S. & Paglione, J. Tuning bulk and surface conduction in the proposed topological Kondo insulator SmB_6 . *Phys. Rev. Lett.* **114**, 096601 (2015).
- Yo, Y. S., Sun, K., Kurdak, Ç., Kim, D.-J. & Fisk, Z. Inverted resistance measurements as a method for characterizing the bulk and surface conductivities of three-dimensional topological insulators. *Phys. Rev. Appl.* **9**, 044006 (2018).
- Zhang, X. et al. Hybridization, inter-ion correlation, and surface states in the Kondo insulator SmB_6 . *Phys. Rev. X* **3**, 011011 (2013).
- Jiang, J. et al. Observation of possible topological in-gap surface states in the Kondo insulator SmB_6 by photoemission. *Nat. Commun.* **4**, 3010 (2013).
- Neupane, M. et al. Surface electronic structure of the topological Kondo-insulator candidate correlated electron system SmB_6 . *Nat. Commun.* **4**, 2991 (2013).
- Dai, W. et al. Proximity-effect-induced superconducting gap in topological surface states – a point contact spectroscopy study of $\text{NbSe}_2/\text{Bi}_2\text{Se}_3$ superconductor-topological insulator heterostructures. *Sci. Rep.* **7**, 7631 (2017).
- Xu, S.-Y. et al. Momentum-space imaging of Cooper pairing in a half-Dirac-gas topological superconductor. *Nat. Phys.* **10**, 943–950 (2014).
- Lee, S. et al. Observation of the superconducting proximity effect in the surface state of SmB_6 thin films. *Phys. Rev. X* **6**, 031031 (2016).
- Borisov, K., Chang, C.-Z., Moodera, J. S. & Stamenov, P. High Fermi-level spin polarization in the $(\text{Bi}_{1-x}\text{Sb}_x)_2\text{Te}_3$ family of topological insulators: a point contact Andreev reflection study. *Phys. Rev. B* **94**, 094415 (2016).
- Shoman, T. et al. Topological proximity effect in a topological insulator hybrid. *Nat. Commun.* **6**, 6547 (2015).
- Hutasoit, J. A. & Stanescu, T. D. Induced spin texture in semiconductor/topological insulator heterostructures. *Phys. Rev. B* **84**, 085103 (2011).
- Szabó, P. et al. Superconducting energy gap of YB_6 studied by point-contact spectroscopy. *Physica C* **460–462**, 626–627 (2007).
- Alexandrov, V., Coleman, P. & Erten, O. Kondo breakdown in topological Kondo insulators. *Phys. Rev. Lett.* **114**, 177202 (2015).
- Wang, M.-X. et al. The coexistence of superconductivity and topological order in the Bi_2Se_3 thin films. *Science* **336**, 52–55 (2012).
- Soulen Jr, R. J. et al. Measuring the spin polarization of a metal with a superconducting point contact. *Science* **282**, 85–88 (1998).
- Strijkers, G. J., Ji, Y., Yang, F. Y., Chien, C. L. & Byers, J. M. Andreev reflections at metal/superconductor point contacts: Measurement and analysis. *Phys. Rev. B* **63**, 104510 (2001).
- Tkachov, G. & Hankiewicz, E. M. Helical Andreev bound states and superconducting Klein tunneling in topological insulator Josephson junctions. *Phys. Rev. B* **88**, 075401 (2013).
- Janvier, C. et al. Coherent manipulation of Andreev states in superconducting atomic contacts. *Science* **349**, 1199–1202 (2015).
- Kornev, V. K., Kolotinskiy, N. V., Levochkina, A. Y. & Mukhanov, O. A. Critical current spread and thermal noise in Bi-SQUID cells and arrays. *IEEE Trans. Appl. Supercond.* **27**, 1601005 (2017).
- Zhang, C., Lu, H.-Z., Shen, S.-Q., Chen, Y. P. & Xiu, F. Towards the manipulation of topological states of matter: a perspective from electron transport. *Sci. Bull. (Beijing)* **63**, 580–594 (2018).

Acknowledgements We thank Y. S. Eo for discussions on the properties of SmB_6 , F. C. Wellstood for discussions on the possible applications of superconducting Klein tunnelling devices, and H. M. Iftexhar Jaim for assistance with X-ray measurements. This project was funded by ONR N00014-13-1-0635; ONR N00014-15-1-2222; AFOSR number FA9550-14-10332; NSF (DMR-1410665); and C-SPIN, one of six centers of STARnet, a Semiconductor Research Corporation (SRC) programme sponsored by MARCO and DARPA. We acknowledge support from the Maryland NanoCenter. J.P. acknowledges support from the Gordon and Betty Moore Foundation's EPiQS Initiative through grant number GBMF4419. V.G. was supported by DOE-BES (DESC0001911) and the Simons Foundation. This work was also supported in part by the Center for Spintronic Materials in Advanced Information Technologies (SMART), one of the centers in nCORE, an SRC programme sponsored by NSF and NIST. The work at University of California, Irvine, was carried out using the electron microscopy facilities

of the Irvine Materials Research Institute (IMRI) and was supported by the National Science Foundation through grant DMR-1506535 and by DOE-BES under grant DE-SC0014430. We acknowledge support from the National Institute of Standards and Technology Cooperative Agreement 70NANB17H301.

Reviewer information *Nature* thanks Ewelina Hankiewicz, David Goldhaber-Gordon and Jinfeng Jia for their contribution to the peer review of this work.

Author contributions S.L., X.Z. and I.T. conceived the experiment. S.L. fabricated thin films and devices, and performed their characterization—including point-contact spectroscopy measurements—with assistance from X.Z. and J.S.H. V.S., V.M.Y. and V.G. performed the theoretical calculations. D.S. analysed the compositions of the films. J.F. performed the literature survey on previous Andreev reflection experiments. S.D., T.B. and X.P. performed TEM measurements. V.M.Y., J.P., R.L.G. and V.G. helped with data interpretation and analysis and manuscript preparation. S.L., V.S., X.Z. and I.T. wrote the paper. I.T.

supervised and coordinated the project. All authors discussed the results and commented on the manuscript

Competing interests The authors declare no competing interests.

Additional information

Extended data is available for this paper at <https://doi.org/10.1038/s41586-019-1305-1>.

Supplementary information is available for this paper at <https://doi.org/10.1038/s41586-019-1305-1>.

Reprints and permissions information is available at <http://www.nature.com/reprints>.

Correspondence and requests for materials should be addressed to I.T.

Publisher's note: Springer Nature remains neutral with regard to jurisdictional claims in published maps and institutional affiliations.

© The Author(s), under exclusive licence to Springer Nature Limited 2019

METHODS

Fabrication of SmB₆ thin film. The growth conditions of SmB₆ thin films have been systematically optimized in order to ensure the quality of SmB₆ thin films. It is known that during the sputtering process, the considerable difference in the atomic masses of Sm and B leads to different scattering probabilities, and thus probably results in a B-deficient film when the deposition is carried out with a stoichiometric target^{21,34,35}. Therefore, we fabricated SmB₆ thin films on Si (001) substrates by co-sputtering SmB₆ and B targets to compensate for possible B deficiency. To remove the native oxide layer on the Si substrate, we treated with hydrofluoric acid (HF) before the thin film deposition. After reaching a base pressure of approximately 2×10^{-8} Torr, the sputtering process was performed on the Si substrates at 860 °C under a deposition pressure of 10 mTorr of Ar (99.999%). The distance between the targets and substrates, as well as the plasma density, were adjusted to increase the activation energy of sputtered species, which is correlated with chemical reaction and atomic migration³⁶. We optimized the power ratio of the two targets for the co-sputtering process by measuring the stoichiometry (that is, the B/Sm ratio) of the deposited SmB₆ thin films using wavelength dispersive spectroscopy (WDS). The optimal powers for SmB₆ and B were found to be 40 W and 60 W, respectively, for a distance between the targets and the substrate of about 10 cm. Under the optimized conditions, the B/Sm ratio of the SmB₆ thin film was 6.0 ± 0.1 . X-ray photoemission spectroscopy and energy-dispersive spectroscopy measurements of the films were used to verify the absence of any impurities that may give rise to metallic conduction at low temperatures. Temperature-dependent resistance measurements show the suggested signature of the emergence of metallic surface states—the saturation of the resistance at low temperatures (that is, resistance plateau) (see Extended Data Fig. 4).

Extended Data Fig. 1a shows a high-resolution transmission electron microscopy image of a cross-section of a SmB₆ sample. There is no indication of the presence of interfacial gradation or extra phases. Extended Data Fig. 1b–d shows selected area electron diffraction (SAED) patterns of the SmB₆ thin film, the Si substrate and the interface regions, respectively. The SAED pattern of the Si substrate (Extended Data Fig. 1c) shows the pattern along the [110] zone axis. In the SAED pattern of the interface (Extended Data Fig. 1d), an additional spot pattern corresponding to the SmB₆ [100] zone orientation (Extended Data Fig. 1b) can be clearly identified (indicated by yellow arrows). The result is indicative of the epitaxial relation, SmB₆ [100] || Si [110], which is consistent with a small lattice mismatch between Si (110) and SmB₆ (100) as illustrated in Extended Data Fig. 1e. Specifically, the *d*-spacing of Si (110) is 3.839 Å, and the lattice mismatch between Si (110) and SmB₆ (100) is about 7%. In addition, aberration-corrected scanning transmission electron microscopy was used, and the atomic-resolution image taken from the SmB₆ film (Extended Data Fig. 1f) reveals its cubic structure. The θ – 2θ X-ray diffraction pattern (Extended Data Fig. 1g) shows a *c*-axis-oriented structure of SmB₆. The XRD diffraction pattern exhibits sharp SmB₆ peaks, which are associated with the {001} planes only. The lattice parameter is found to be 4.13 Å, which is close to the bulk value¹⁴.

Fabrication of superconducting YB₆ thin films and the effect of stoichiometry on *T_c*. Yttrium hexaboride (YB₆) is a known rare-earth hexaboride superconductor with a bulk zero resistance *T_c* of around 7 K^{25,37}. It has been reported that the superconducting properties of YB₆ are closely related to the composition³⁸. However, a systematic study of the superconducting properties with broad variation in composition has not been previously reported. We have successfully fabricated superconducting YB_{6±δ} films for the first time. To achieve the highest *T_c* in YB_{6±δ} thin films for the present study, we first studied the effect of the stoichiometry on the *T_c* of sputtered YB_x thin films. Owing to the substantial difference in the atomic masses between Y and B, and the variation in the distance from the target to different locations of a 3" wafer, we were able to fabricate 'natural composition spread' films of YB_x by sputtering a stoichiometric YB₆ target. Similar to the deposition and the characterization of SmB₆ thin films, a deposition pressure of 10 mTorr and a growth temperature of 860 °C were used for YB_{6±x} thin film growth on Si (001) substrates. The distance between the YB₆ target and the Si substrate was about 10 cm, and the d.c. power applied to the YB₆ target was 60 W. The stoichiometric B/Y ratio for films deposited at different positions was examined by WDS measurements. As shown in Extended Data Fig. 2a, the temperature dependence of the normalized resistance (R/R_N , where *R_N* is the normal state resistance) of the YB_x thin films indicates that the superconducting transition temperature *T_c* varies with the stoichiometric B/Y ratio. In Extended Data Fig. 2b, *T_c* is plotted as a function of the stoichiometric B/Y ratio. The highest *T_c* is observed in the slightly boron-deficient region (B/Y = 5.6). Thus, YB_{5.6} films were used for the present study, and for simplicity, the YB_{5.6} films used in this study are referred to as YB₆ films. The SmB₆/YB₆ heterostructures were fabricated through a sequential high-temperature deposition process without breaking the vacuum—that is, an in situ process as described in the main text—to ensure a pristine interface between SmB₆ and YB_{5.6}²¹. YB₆ has a cubic structure with almost the same lattice constant as SmB₆ (about 4.1 Å) (YB₆; JCPDS number

16-0732 and SmB₆; JCPDS number 36-1326), and thus lattice mismatch strain is expected to be negligible.

Fabrication of Au-SmB₆/YB₆ structures and the temperature dependence of *dI/dV* curves. The analysis of the temperature dependence of *dI/dV* spectra can be used to verify that the gap-like feature is indeed attributed to the proximity-induced superconductivity. To perform a systematic temperature-dependence measurement, Au-SmB₆/YB₆ structures were fabricated using a method including multiple photolithography and ion-milling processes. Microposit S1813 was used as the photoresist, and after spin-coating the photoresist was baked at 100 °C for 2 min. After exposure to ultraviolet light, the samples were developed using a Microposit CD-26 developer for 60 s. A schematic cross-sectional structure of the thin-film devices is shown in Extended Data Fig. 3a. The SmB₆/YB₆ heterostructure was subject to in situ Ar plasma cleaning before Au deposition. After the Au deposition, two rounds of photolithography and ion-milling processes were carried out to define the line shape and the circular junction area, respectively. A SiO₂ (100 nm) layer was used to electrically isolate a top electrode from the SmB₆/YB₆ line. The top electrode, consisting of Au, was fabricated through a lift-off process. The optical microscope image (Extended Data Fig. 3b) shows the top view of a Au-SmB₆/YB₆ structure with a circular junction (diameter, 10 μm).

Extended Data Fig. 3c shows normalized *dI/dV* spectra of the Au-SmB₆ (20 nm)/YB₆ structure at different temperatures (1.8–4.5 K). The enhancement in conductance due to Andreev reflection is approximately 1.8, which is slightly smaller than the value obtained from junctions in the point-contact configuration as described in the main text. Given the specific geometric design of the junction, quasiparticle lifetime broadening^{39,40} and/or an oblique angle for incident electrons may lead to a slightly reduced zero-bias conductance enhancement (see Supplementary Discussion). In the former case, for example—as shown in Extended Data Fig. 3c—by introducing a lifetime broadening term Γ with a value of less than 10% of Δ , we can fit the data using the Dirac–BTK model. The Δ values obtained by the Dirac–BTK fits to the *dI/dV* spectra at different temperatures agree well with those from point-contact spectroscopy measurements carried out with a PtIr tip.

Comparison of SmB₆ and Y-substituted SmB₆. To confirm that the absence of bulk gapless states is crucial for the perfect conductance doubling observed in point-contact spectroscopy measurements, we modified the bulk electronic structure of SmB₆ by Y substitution. Specifically, we performed point-contact spectroscopy measurements on Sm_{1–x}Y_xB₆/YB₆ heterostructures. Y-substituted SmB₆ heterostructures were prepared by co-sputtering SmB₆, B and YB₆ targets, and the composition was determined by WDS. Extended Data Fig. 4a shows the resistance normalized by the value at 300 K (R/R_{300K} , logarithmic scale) plotted against the inverse of temperature ($1/T$) plots of SmB₆ as well as 20% and 50% Y-substituted SmB₆ (Sm_{0.8}Y_{0.2}B₆ and Sm_{0.5}Y_{0.5}B₆) thin films. The behaviour of the temperature-dependent resistance of the bulk states can be described by an exponential function, $R_{\text{bulk}}(T) \propto \exp(E_a/k_B T)$, where *E_a* and *k_B* are a carrier activation energy and Boltzmann constant, respectively. Hence the positive linear slopes in the relatively high-temperature region in Extended Data Fig. 4a are approximately proportional to the corresponding activation energies. The slope decreases with increasing Y concentration, which implies that Y-substitution increases the bulk conductivity and reduces the activation energy of carriers. More explicitly, in order to estimate and provide the activation energies of SmB₆ and Sm_{0.8}Y_{0.2}B₆, only the bulk conductance channel should be taken into account. Thus, based on a simple parallel conductance model (total $G = G_{\text{bulk}} + G_{\text{surface}}$) below the temperature at which the Kondo gap is completely open (roughly 40 K)^{14,16,21,35,41}, we plot $G - G_{\text{surface}}$ (logarithmic scale) against $1/T$ in Extended Data Fig. 4b, where G_{surface} is modelled as a linear function of temperature⁴¹, and $G - G_{\text{surface}}$ is normalized by *G* at 300 K. Now the slopes of $G - G_{\text{surface}}$ in Extended Data Fig. 4b correspond to the activation energies of pure SmB₆ and Sm_{0.8}Y_{0.2}B₆, which are found to be 3.0 meV and 2.2 meV, respectively.

Details of the point-contact spectroscopy measurements. PCAR measurements were carried out using a probe built in-house and designed for operation in a physical property measurement system (Quantum Design). Using a mechanically sharpened tip, point-contact junctions with a contact resistance of few ohms were achieved by gently approaching the tip onto the surface of the heterostructure at 2 K. In order to demonstrate the robustness of perfect Andreev reflection observed in the SmB₆ (20–30 nm)/YB₆ heterostructures, we made multiple contact measurements by lifting up the PtIr tip and repositioning it to land at other spots (position 1–3) on the same samples. As shown in Extended Data Fig. 5, in each set of such measurements, we consistently obtained conductance doubling for all contacts made on SmB₆ (20–30 nm)/YB₆ heterostructures despite the expected local variation in the surface microstructure.

Conductance enhancement against Z-barrier strength. There are many factors that cause scattering and thus contribute to the barrier strength *Z* in the standard BTK theory^{9,10}. In point-contact spectroscopy experiments, it is often difficult to avoid the formation of an oxide layer at the surface. Even when the interface is

formed in situ under vacuum for thin-film devices, the interfaces are defined as where the two disparate materials meet: the difference in the crystal structure and the atomic-level surface microstructure, including facets and terminations, can lead to structural and compositional disorder and defects serving as scattering centres. Mechanical point contacts have an added complication due to local deformation of the tip. Furthermore, Fermi velocity mismatch also affects the reflection and transmission probabilities. Therefore, Z is finite for almost all normal metal-topologically trivial superconductor junctions, which leads to conductance enhancements of considerably less than two.

To illustrate the uniqueness of the perfect Andreev reflection that is evident here in the doubled conductance (normalized $dI/dV = 2$) and the difficulty in general in observing such a high conductance enhancement, we surveyed the open literature on point-contact spectroscopy measurements on various superconductors. Because Z is a primary parameter associated with the conductance enhancement in the standard BTK theory⁹, we plot normalized dI/dV at zero bias against Z (Fig. 3). We looked at over 250 publications on point-contact spectroscopy measurements and selected data points from 44 reports using three criteria: (1) the value of Z is extracted using a BTK fit; (2) the conductance enhancement is larger than 1 (normalized $dI/dV \geq 1$), which indicates that a particular junction is not in the tunnel-dominant regime; and (3) the conductance enhancement is not governed by any zero-bias conductance peak due to a nodal order parameter. For the plot in Fig. 3 we display the data points in the range of $0 \leq Z \leq 0.8$. Detailed information—including the types of superconductors, contacts and their references—are summarized in Supplementary Table.

Comparison of dI/dV spectra in standard BTK and Dirac-BTK models. Extended Data Fig. 6a shows a comparison of dI/dV curves according to the standard BTK and the Dirac-BTK models for different Z values, from which it can be clearly seen how the dI/dV spectrum is modified by changing the barrier strength Z . In the standard BTK model, the conductance within the superconducting gap gradually decreases with increasing Z , whereas the dI/dV spectra in the Dirac-BTK model remain unchanged regardless of the value of Z , as theoretically described in the main text. Such dependency is also captured in the curves in Fig. 3 (that is, normalized dI/dV at zero bias against Z according to the standard BTK and the Dirac-BTK models). Extended Data Fig. 6b shows the comparison of the Dirac-BTK and the standard BTK fits to the dI/dV spectrum of a PtIr-SmB₆ (20 nm)/YB₆ contact. When the standard BTK model is used, as expected, the best fit is obtained by setting $Z = 0$, which then provides an identical fit to the Dirac-BTK (with the same Δ). If we use a more realistic value, $Z = 0.39$, the standard BTK gives a fit with considerable deviation from the experimental curve. As discussed in the main text, $Z = 0.39$ was extracted from spectra of heterostructures that are similar in terms of materials but do not have complete topological protection, namely SmB₆ (10 nm)/YB₆ and Y-substituted SmB₆/YB₆ heterostructures. The plot clearly demonstrates that the standard BTK model with a finite and realistic Z cannot reproduce the experimental data that show the perfect Andreev reflection.

Magnetic-field-dependent dI/dV spectra of a point contact with a SmB₆/YB₆ heterostructure. Applying a magnetic field can break time-reversal symmetry, and the effect can be used as a signature of the perfect Andreev reflection due to Klein tunnelling. We measured the field-dependent dI/dV spectrum of a device with a thin-film Au layer as a normal metal (that is, Au-SmB₆/YB₆ structure; see Extended Data Fig. 3) that provides a stable contact under an applied magnetic field, as opposed to a point-contact junction which can potentially suffer from magnetostriiction. As shown in Extended Data Fig. 7a, the enhancement of conductance is gradually suppressed with increasing magnetic field in both out-of-plane and in-plane field configurations, but the normalized dI/dV at zero bias decreases more quickly when the magnetic field is applied along the out-of-plane direction compared to when it is applied in-plane (Extended Data Fig. 7b). However, the decreasing trend of the superconducting gap (Δ) due to applied field is approximately the same for the out-of-plane and in-plane directions (inset of Extended Data Fig. 7b). The fact that the conductance is suppressed more quickly under the out-of-plane field thus cannot be explained solely by field-induced diminishing of superconductivity in the SmB₆/YB₆ heterostructure.

The effect of magnetic field on the helical surface states depends on factors such as the direction of the field, the position of the Fermi level relative to the Dirac point, and the magnitude of the effective g -factor. Applying the magnetic field parallel to the surface will distort and shift the Dirac cone, but without affecting the spin-momentum locking at the Fermi level^{42,43}. However, a magnetic-field component perpendicular to the surface will open a gap at the Dirac point and a back-scattering channel by inducing a z -component of the electron spins⁴²⁻⁴⁴. In other words, we expect considerable suppression of the conductance when the field is applied out of plane, which is consistent with our observation here.

The observed suppression, however, is not especially pronounced in either direction, and we attribute this to the small effective g -factor of the surface states in SmB₆. The size of the opened gap or the shift in Fermi surface (Δ_B) due to the magnetic field B is proportional to the Zeeman energy, $\Delta_B = g_{\text{eff}}\mu_B B$, where g_{eff}

is the effective g -factor of surface states and μ_B is the Bohr magneton⁴⁵. Thus, for sufficiently small g_{eff} , the application of B does not weaken topological protection substantially, provided that the Fermi level is sufficiently far away from the Dirac point. To the best of our knowledge, the effective g -factor for the surface states of SmB₆ has not been reported, but the value for the bulk states of SmB₆ has been estimated to be around 0.1^{46,47}. It has been reported that the effective g -factor of surface states of Bi₂Se₃ is similar to the bulk value in Bi₂Se₃ ($g_{\text{eff}} \approx 50$)⁴⁸. In the absence of a directly measured value for SmB₆ and assuming that its behaviour is similar to that of Bi₂Se₃, we take the g -factor of the surface states of SmB₆ to also be around 0.1.

Recent magnetoresistance studies on SmB₆ also suggest a small effective g -factor for the surface states of SmB₆^{47,49,50}. For example, a very weak field-dependence of the resistance at low temperatures (for instance, $\Delta R/R \approx 2\%$ for 80 T at 1.39 K) has been reported⁴⁷, which suggests that the surface states of SmB₆ are extremely robust against an applied magnetic field. This is consistent with the gradual suppression of conductance enhancement by magnetic fields that we have observed here.

Conductance doubling and conductance dip near the gap. To the best of our knowledge, there have been only two reports in the literature in which the observed conductance enhancement is larger than 1.9. They are both on Nb-Cu point contacts^{28,29} (also see Fig. 3 and Supplementary Table). The spectra showing conductance doubling therein are reproduced in Extended Data Fig. 8, and one of our PtIr-SmB₆ (20 nm)/YB₆ spectra is also shown in the figure for comparison. The reported Nb-Cu spectra exhibit distinctive features—namely, conductance dips near the bias voltage corresponding to the superconducting gap energy of Nb (indicated by arrows in Extended Data Fig. 8). These dips cannot be reproduced using the standard BTK theory alone. A model has been proposed to account for the dips that are intimately tied to the conductance doubling²⁹. In this model, when Z is exceptionally small due to a negligible Fermi velocity mismatch—as in the special case of Nb-Cu junctions—the interface becomes effectively transparent, which enables the superconducting proximity effect to create a region in the normal metal side with a superconducting order parameter (Δ_{prox}) that is smaller than the order parameter of the superconductor. In such an instance, the Andreev reflection process is limited to the energy of incident particles within $|\Delta_{\text{prox}}|$. According to the model put forth in ref. 29, because the quasiparticles in the proximitized layer on the normal metal side can enter the superconductor side only when their energy is outside the energy gap of the superconductor, the dI/dV spectrum develops large conductance dips near voltages that roughly correspond to the gap energy of the superconductor. Therefore, we attribute the substantial dip feature to $Z \approx 0$ in the case of Nb-Cu junctions. The absence of such a feature in our results thus indicates that the perfect conductance doubling observed in the PtIr-SmB₆ (20–30 nm)/YB₆ junctions is of a different origin compared to that in the Nb-Cu contacts. In the case of a contact between PtIr and SmB₆, a substantial barrier is expected just on the basis of the substantial Fermi velocity mismatch between them (the Fermi velocity of the surface states of SmB₆ is $< 10^5 \text{ m s}^{-1}$)^{17,18,21}. This underscores the need for an alternative model to explain the perfect Andreev reflection observed in the PtIr-SmB₆/YB₆ heterostructures here.

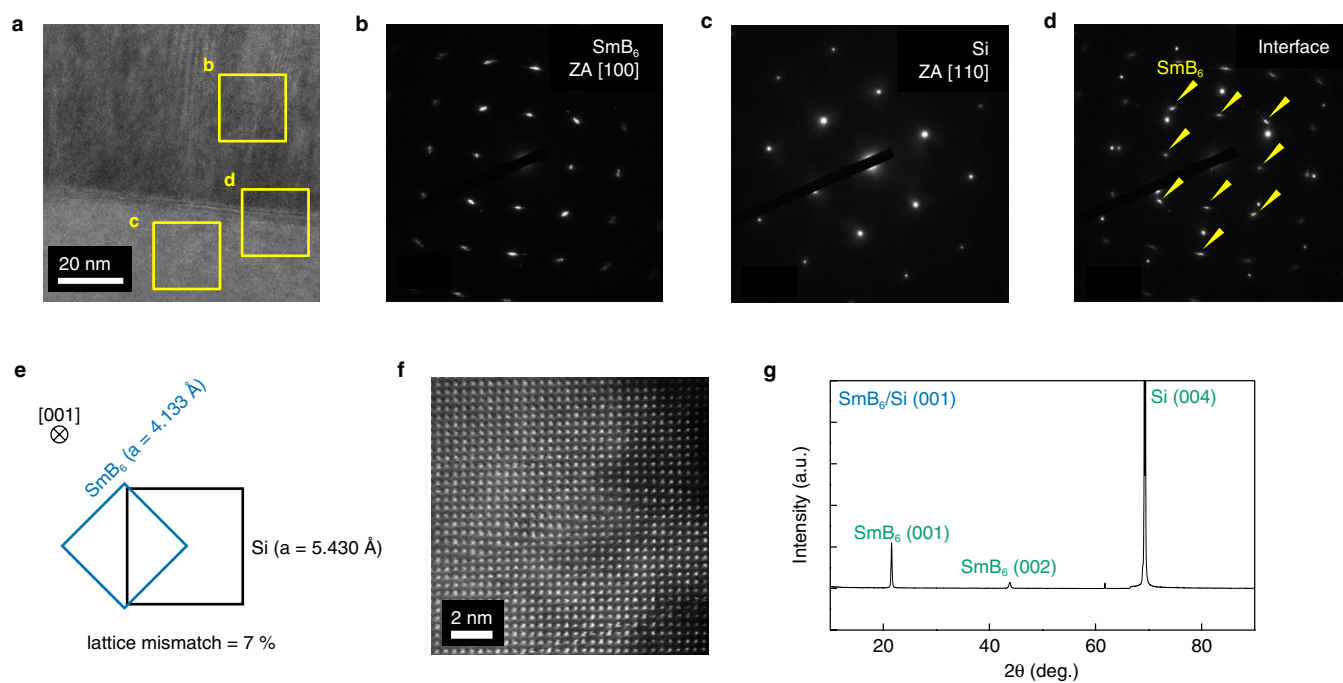
Note that shallow dips observed in the dI/dV spectra of our PtIr-SmB₆ (20 nm)/YB₆ junctions are common to dI/dV spectra of various normal metal–superconductor junctions (for example, refs 10,51–54). They are attributed to the inhomogeneous nature of point contact, which can consist of many parallel channels—in some of which excessive current can flow^{10,55}.

Data availability

The data that support the findings of this study are available within the paper. Additional data are available from the corresponding authors upon reasonable request.

- Yong, J. et al. Robust topological surface state in Kondo insulator SmB₆ thin films. *Appl. Phys. Lett.* **105**, 222403 (2014).
- Li, Y., Ma, Q., Huang, S. X. & Chien, C. L. Thin films of topological Kondo insulator candidate SmB₆: strong spin-orbit torque without exclusive surface conduction. *Sci. Adv.* **4**, eaap8294 (2018).
- Ohring, M. *Materials science of thin films* 2nd edn (Academic, 2001).
- Schneider, R., Geerk, J. & Rietschel, H. Electron tunnelling into a superconducting cluster compound: YB₆. *Eur. Phys. J. Lett.* **4**, 845–849 (1987).
- Sluchanko, N. et al. Lattice instability and enhancement of superconductivity in YB₆. *Phys. Rev. B* **96**, 144501 (2017).
- Dynes, R. C., Narayanamurti, V. & Garno, J. P. Direct measurement of quasiparticle-lifetime broadening in a strong-coupled superconductor. *Phys. Rev. Lett.* **41**, 1509–1512 (1978).
- Mazin, I. I., Golubov, A. A. & Nadgorny, B. Probing spin polarization with Andreev reflection: a theoretical basis. *J. Appl. Phys.* **89**, 7576–7578 (2001).
- Wolgast, S. et al. Low-temperature surface conduction in the Kondo insulator SmB₆. *Phys. Rev. B* **88**, 180405 (2013).
- Taskin, A. A. et al. Planar Hall effect from the surface of topological insulators. *Nat. Commun.* **8**, 1340 (2017).
- Wang, L.-X. et al. Zeeman effect on surface electron transport in topological insulator Bi₂Se₃ nanoribbons. *Nanoscale* **7**, 16687–16694 (2015).

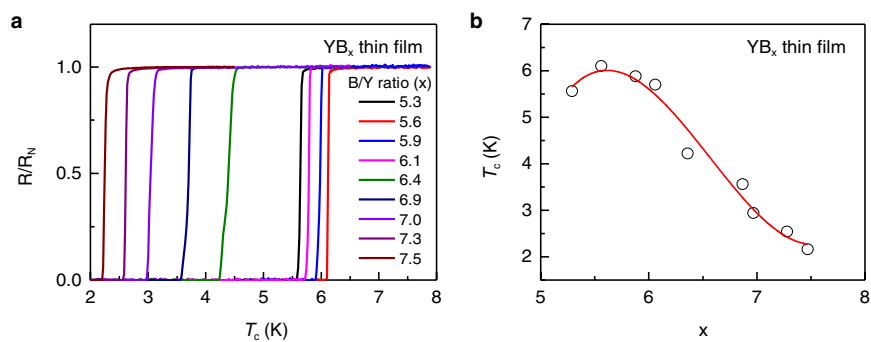
44. Chang, C.-Z., Wei, P. & Moodera, J. S. Breaking time reversal symmetry in topological insulators. *MRS Bull.* **39**, 867–872 (2014).
45. Fu, Y.-S. et al. Observation of Zeeman effect in topological surface state with distinct material dependence. *Nat. Commun.* **7**, 10829 (2016).
46. Erten, O., Ghaemi, P. & Coleman, P. Kondo breakdown and quantum oscillations in SmB_6 . *Phys. Rev. Lett.* **116**, 046403 (2016).
47. Wolgast, S. et al. Reduction of the low-temperature bulk gap in samarium hexaboride under high magnetic fields. *Phys. Rev. B* **95**, 245112 (2017).
48. Analytis, J. G. et al. Transport in the quantum limit by two-dimensional Dirac fermions in a topological insulator. *Nat. Phys.* **6**, 960–964 (2010).
49. Thomas, S. et al. Weak antilocalization and linear magnetoresistance in the surface state of SmB_6 . *Phys. Rev. B* **94**, 205114 (2016).
50. Biswas, S. et al. Robust local and nonlocal transport in the topological Kondo insulator SmB_6 in the presence of a high magnetic field. *Phys. Rev. B* **92**, 085103 (2015).
51. Gonnelli, R. S. et al. Temperature and junction-type dependency of Andreev reflection in MgB_2 . *J. Phys. Chem. Solids* **63**, 2319–2323 (2002).
52. Li, Z.-Z. et al. Andreev reflection spectroscopy evidence for multiple gaps in MgB_2 . *Phys. Rev. B* **66**, 064513 (2002).
53. Park, W. K., Greene, L. H., Sarrao, J. L. & Thompson, J. D. Andreev reflection at the normal-metal/heavy-fermion superconductor CeCoIn_5 interface. *Phys. Rev. B* **72**, 052509 (2005).
54. Zhang, X. et al. Evidence of a universal and isotropic $2\Delta/k_B T_C$ ratio in 122-type iron pnictide superconductors over a wide doping range. *Phys. Rev. B* **82**, 020515 (2010).
55. Sheet, G., Mukhopadhyay, S. & Raychaudhuri, P. Role of critical current on the point-contact Andreev reflection spectra between a normal metal and a superconductor. *Phys. Rev. B* **69**, 134507 (2004).



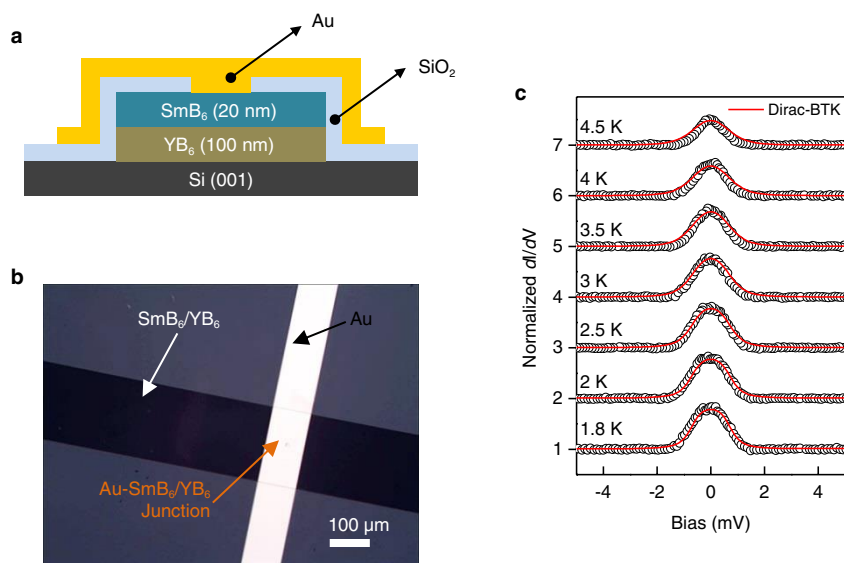
Extended Data Fig. 1 | Structural characterization of SmB₆ thin films.

a, High-resolution cross-sectional transmission electron microscopy image of a SmB₆ thin film. The yellow squares correspond to the regions of the SAED measurements shown in **b–d**. **b–d**, SAED measurements of SmB₆ (**b**), Si substrate (**c**) and SmB₆/Si interface regions (**d**). ZA, zone

axis. **e**, Epitaxial relationship between the SmB₆ and the Si substrate. **f**, Aberration-corrected scanning transmission electron microscopy cross-sectional image of a SmB₆ thin film. **g**, θ - 2θ X-ray diffraction pattern of a SmB₆ thin film on a Si (001) substrate.

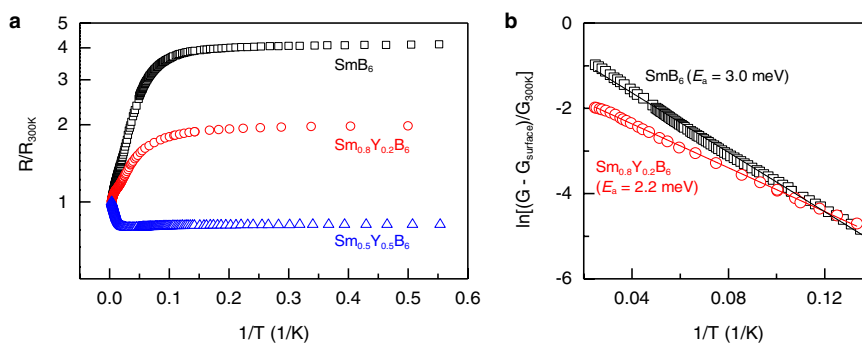


Extended Data Fig. 2 | Superconducting transition temperature (T_c) of YB_x thin films. **a**, Temperature-dependent resistance curves of YB_x thin films with different stoichiometric B/Y ratios. **b**, Change in T_c as a function of stoichiometric B/Y ratio (x).



Extended Data Fig. 3 | Au-SmB₆/YB₆ thin film junctions. **a**, Cross-sectional schematic of a Au-SmB₆ (20 nm)/YB₆ (100 nm) structure. **b**, Optical microscopy image of the device. **c**, Normalized dI/dV spectra of the Au-SmB₆/YB₆ structure at different temperatures. The red lines are

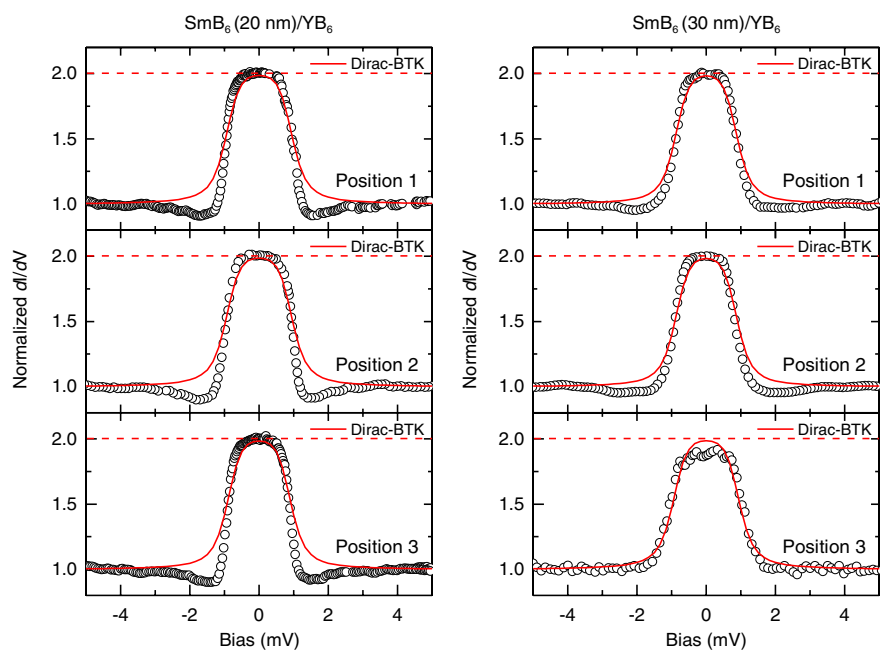
fits using the Dirac-BTK model. The normalized dI/dV curves at 1.8 K are plotted using the obtained values, whereas the other curves are vertically shifted for clarity.



Extended Data Fig. 4 | Yttrium-substituted SmB_6 thin films.

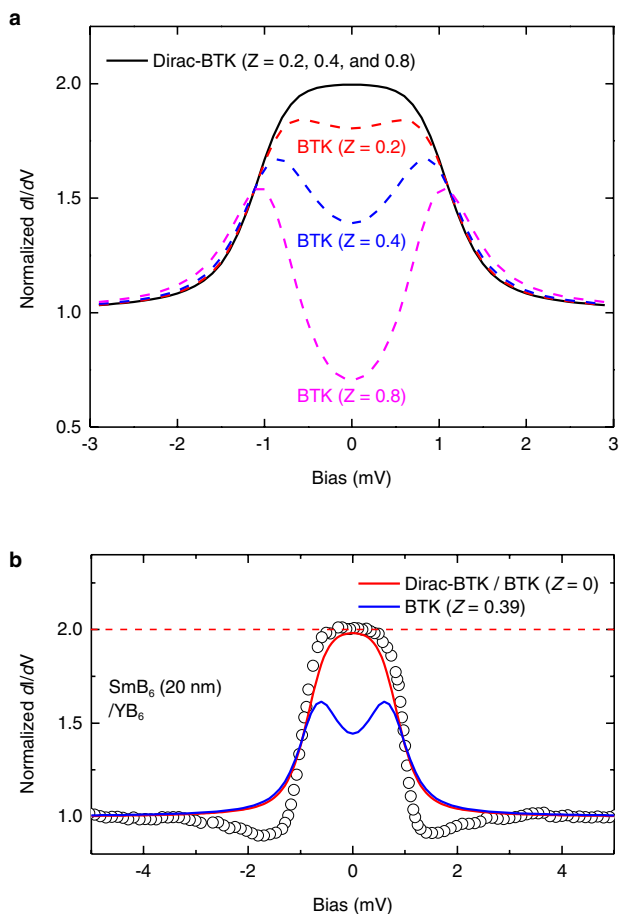
a, Comparison of $\log R$ against $1/T$ plots of SmB_6 , and 20% and 50% Y-substituted SmB_6 (that is, $Sm_{0.8}Y_{0.2}B_6$ and $Sm_{0.5}Y_{0.5}B_6$, respectively). The resistance values are normalized by their values at 300 K. The positive linear slopes at in the relatively high-temperature regions are roughly

proportional to the activation energy. **b**, $G - G_{surface}$ (logarithmic scale, normalized by the conductance at 300 K) plotted against $1/T$ for pure SmB_6 (black squares) and $Sm_{0.8}Y_{0.2}B_6$ (red circles). The slopes of the linear fits (black and red lines) correspond to the activation energies (E_a) of pure SmB_6 and $Sm_{0.8}Y_{0.2}B_6$, and are 3.0 meV and 2.2 meV, respectively.

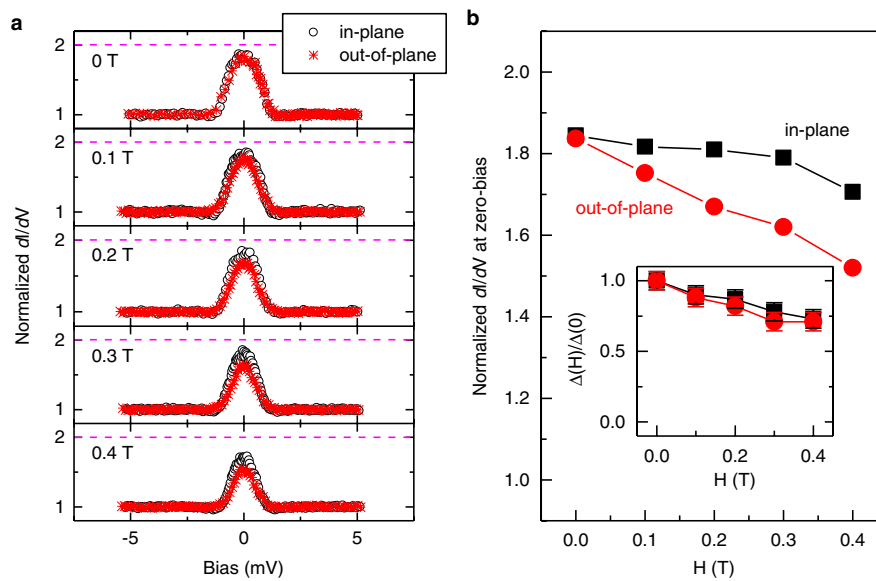


Extended Data Fig. 5 | Robustness of perfect Andreev reflection.
Point-contact spectra obtained at different positions (1, 2 and 3, which are roughly 1 mm apart from each other) on SmB_6/YB_6 heterostructures

with 20-nm-thick SmB_6 (left) and 30-nm-thick SmB_6 (right). Conductance doubling is consistently observed at all positions in the dI/dV spectra of the SmB_6/YB_6 heterostructures.

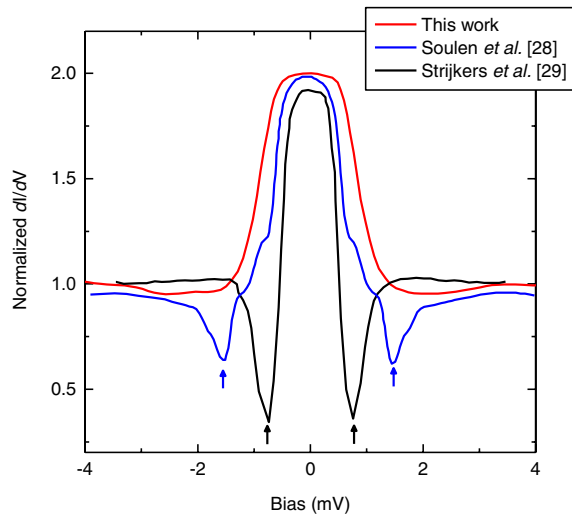


Extended Data Fig. 6 | Standard BTK compared with Dirac-BTK models. **a**, Comparison of calculated dI/dV spectra with the standard BTK and the Dirac-BTK models for $Z = 0.2, 0.4$ and 0.8 ($\Delta = 1$ meV). **b**, Comparison of the Dirac-BTK and the standard BTK fits to the experimental dI/dV spectrum of a PtIr-SmB₆ (20 nm)/YB₆ contact (Fig. 1c). The red curve is the theoretical conductance curve in the Dirac-BTK model and the standard BTK model with $Z = 0$. Both appear identical, as expected, for the same Δ (here 0.77). The blue curve is the theoretical standard BTK curve with $\Delta = 0.77$ and $Z = 0.39$, this Z value is assessed from contacts to other heterostructures in this study that do not exhibit perfect Andreev reflection (that is, those with thin SmB₆ (10 nm) and Y-substituted SmB₆). The effect of nullifying Z by incorporation of a Dirac material in the Andreev reflection process is clearly seen.



Extended Data Fig. 7 | Magnetic-field-dependent dI/dV spectra. **a**, dI/dV spectra of Au-SmB₆/YB₆ device under a magnetic field applied along the in-plane and out-of-plane directions. **b**, Normalized dI/dV at zero bias as a function of magnetic field. The inset shows superconducting order

parameter (Δ) as a function of magnetic field normalized by Δ at 0 T ($\Delta(0)$). Δ was estimated as the bias voltage point at which the maximum first derivative of each dI/dV spectrum occurs under different magnetic fields.



Extended Data Fig. 8 | Experimentally observed conductance doubling.

Comparison of the normalized dI/dV spectrum obtained from the PtIr-SmB₆ (20 nm)/YB₆ junction in this work (red line, experimental data) with the reported point-contact spectra obtained from Nb-Cu junctions^{28,29}. The arrows indicate conductance dips near the Δ . Such dips are not present in our spectrum.